ACS OMEGA

Open Access

http://pubs.acs.org/journal/acsodf

Article

Coal Tar Pitch-Based Porous Carbon Loaded MoS_2 and Its Application in Supercapacitors

Rui Bai, Yuan-Jia Cao, Cui-Ying Lu,* and Guang-Hui Liu

Cite This: *ACS Omega* 2023, 8, 34471−34480

Read Online

ACCESS | Metrics & More | Article Recommendations | Supporting Information

ABSTRACT: In this paper, with coal tar pitch as the carbon source, porous carbon (PC) was prepared by one-step carbonization. To improve the energy density of coal tar pitch-based porous carbon, MoS_2@PC was prepared by a hydrothermal method on a PC substrate. The effect of MoS_2 loading on the structure and electrochemical properties of the sample was studied. The results show that the specific surface area of the MoS_2@PC-0.3 synthesized is 3053 m^2 g^{-1}, and the large specific surface area provides sufficient attachment sites for the storage of electrolyte ions. In the three-electrode system, the specific capacitance of MoS_2@PC-0.3 at 0.5 A g^{-1} is 422.5 F g^{-1}, and the magnification performance is 57.3% at 20 A g^{-1}. After 10,000 charge/discharge cycles, the capacitance retention rate of the sample is 76.73%, with the Coulombic efficiency being 100%. In the two-electrode test system, the specific capacitance of MoS_2@PC-0.3 at 0.5 A g^{-1} is 321.4 F g^{-1}, with the power density and energy density being 500 W kg^{-1} and 44.6 Wh kg^{-1}, respectively. At a current density of 20 A g^{-1}, the capacitance retention rate is 87.69% after 10,000 cycles. This study greatly improves the energy density of PC as the electrode material of supercapacitors.

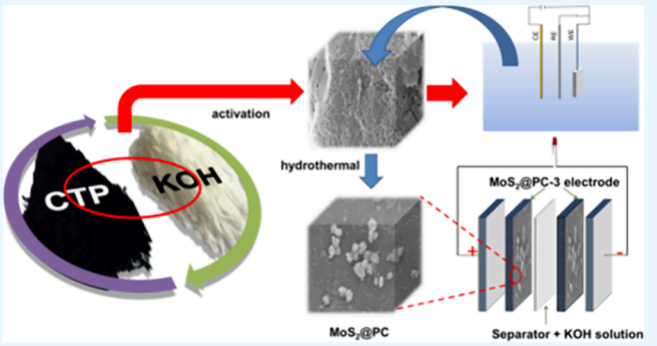

1. INTRODUCTION

Supercapacitors (SCs) have attracted wide attention due to their high power density,[1] long cycle life,[2] and fast charge/discharge rate.[3] However, the disadvantage of supercapacitors is equally obvious: the limited energy density, which seriously hinders the industrial application of SCs in energy consumption devices.[4,5] It is well known that the energy density of SCs is mainly related to the capacitive behavior of electrode materials.[6,7] Therefore, to improve the energy density, it is an urgent task to develop efficient and novel SC electrode materials.[8,9]

In recent years, the application of two-dimensional layered nanostructures, especially MoS_2 in batteries and supercapacitors,[10,11] has been widely studied. It has good in-plane covalent bonds, resulting in special mechanical elasticity in the layer and outstanding robustness along the *C* axis.[12] Because of different interlayer interactions, MoS_2 also consists of three types, namely, 1 T, 2 H, and 3 Re MoS_2.[13] However, pure MoS_2 as an electrode material has the disadvantages of easy agglomeration and low conductivity. To solve these problems of MoS_2, some scholars used graphene, carbon nanotubes, porous carbon, and other[14−17] nanomaterials to composite with MoS_2 to optimize its electrochemical performance as an electrode material for supercapacitors. The special structure of the composite can uniformly disperse MoS_2 and expose more reactive sites, thus improving the electrochemical performance. In addition, PC used in supercapacitors has the disadvantage of low energy density, and the advantage of high energy density of MoS_2 can well neutralize this shortcoming so as to achieve the purpose of improving the electrochemical performance of composite materials. By means of magnetron sputtering technology, Tiwari et al.[18] directly grew ultrathin MoS_2 nanoflakes on carbon nanotubes prepared by chemical vapor deposition. The asymmetric supercapacitor assembled with this as the working electrode displays a high volume specific capacity. Fu et al.[19] prepared three-dimensional spongy polyaniline (PANI) using SiO_2 as a hard template and then added polyvinylpyrrolidone (PVP) during the growth of MoS_2 to obtain a high-energy-density sPANI/A-MoS_2 composite. Lin et al.[20] used a hydrothermal method to grow MoS_2 nanosheets on the layered porous carbon derived from pomelo peel. At a current density of 0.5 A g^{-1}, the specific capacitance was 411.4 F g^{-1}. Wang et al.[21] combined MoS_2 with porous carbon derived from corncobs, and the prepared electrode material possessed a specific capacitance of 333.5 F g^{-1} at a current density of 1 A g^{-1}. Sangeetha and Selvakumar[22] prepared

Received: April 27, 2023
Accepted: September 6, 2023
Published: September 15, 2023

carbonized tendu/MoS_2 composites with the specific capacitances of three-electrode properties attaining 193 F g^{-1} at the optimum ratio. Lin et al.[23] synthesized the sandwich-like composites of carbonized popcorn and MoS_2 by a hydrothermal method. The highest reversible capacity was as high as 475 mAh g^{-1} at a current density of 0.2 A g^{-1}. As shown by the above research, it is feasible to load MoS_2 with carbon materials.

In addition, as a byproduct of the semicoke industry, China's medium- and low-temperature coal tar has an annual capacity of about 6.2 million tons. The production capacity of medium- and low-temperature coal tar asphalt in Yulin is about 3.68 million tons, accounting for 60% of the national production capacity. However, medium- and low-temperature coal tar pitch is mostly used as infrastructure materials and heavy fuel oil, resulting in serious waste of carbon resources and environmental pollution.[24] Therefore, how to improve the utilization of high-value-added products based on coal tar pitch has become an urgent problem to be solved.

In this case, this paper uses coal tar pitch-based porous carbon as the substrate to prepare MoS_2@PC composites by the hydrothermal method. PC has the characteristics of a high specific surface area and rich pore structure, providing sufficient growth space for loaded MoS_2. The results show that the electrochemical properties of MoS_2@PC composites are significantly improved compared with those of PC.

2. EXPERIMENTAL SECTION

2.1. Materials. The low-temperature CTP (softening point 176 °C) was provided by Yulin Coal Chemical Industry Upgrade Technology R&D Center. CTP was pulverized to pass through a 200-mesh sieve (particle size ≤74 μm) followed by vacuum desiccation at 80 °C for 24 h before use. Polytetrafluoroethylene (PTFE) was purchased from Aladdin Chemical Co. Ltd., China. KOH (85 wt %) and HCl solution (37 wt %) were purchased from Shanghai Chemical Reagent Co. Ltd., China. Ethanol, which is analytically pure, was purchased from Tianjin Kemiou Chemical Reagent Co., Ltd. Ammonium molybdate and thiourea, also analytically pure, were purchased from Tianjin Binhai Kedi Chemical Reagent Co., Ltd., and Tianjin Yongsheng Fine Chemical Co., Ltd., respectively.

2.2. Synthesis of MoS_2@PC. MoS_2 was prepared by adding thiourea and ammonium molybdate according to the molar ratio of sulfur/molecular nitrogen (a ratio of 2:1). A certain amount of thiourea and ammonium molybdate was dissolved in 80 mL of deionized water for ultrasound for 10 min and then placed in 200 mL of polytetrafluoroethylene lining for 24 h in a 220 °C drying oven. After the sample was cooled to room temperature, the supernatant was poured out, centrifuged with anhydrous ethanol and deionized water three times, and dried at 105 °C for 12 h to obtain MoS_2.

A certain amount of PC (Supporting Information) and ammonium molybdate was weighed and dissolved in 80 mL of deionized water (the mass ratio of MoS_2 and PC is M = 0.2, 0.3, and 0.4, and the mass of MoS_2 is calculated according to the conversion rate of 100%). The subsequent steps were consistent with the process of preparing MoS_2. The obtained sample was named as MoS_2@PC-M.

2.3. Characterization. Under 77 K, the hole structure of MOS_2@PC-M was characterized by N_2 adsorption (Micromeritics Asap 2460). The SSA and the aperture distribution were determined by Brunauer–Emmett–Teller (BET) and density functional theory (DFT) methods, respectively. The microstructure and surface shape of MOS_2@PC-M were studied with a scanning electronic microscope (SEM, Sigma300) under 10 kV acceleration voltage. The internal structure of MoS_2@PC-M was determined by transmission electron microscopy and high-resolution transmission electron microscopy (TEM and HRTEM, Talos F200X G2, superX). The samples were characterized using an X-ray diffractometer (XRD, Bruker D8 Advance). The Raman spectrum in the range of 400–4000 cm^{-1} was recorded using a HORIBA Scientific LabRAM HR Evolution laser confocal Raman spectrometer. X-ray photoelectron spectroscopy (XPS, Thermo Scientific K-Alpha) was used to detect the content and distribution of elements in MoS_2@PC-M.

2.4. Electrochemical Measurements. A total of 1–2 mg of MoS_2@PC-M, polytetrafluoroethylene (PTFE), and acetylene black were mixed in 10 mL of ethanol solution at 8:1:1 mass ratio to obtain a working electrode slurry. The slurry was applied on 1 × 1 cm^2 pretreated foam nickel and then dried for 24 h in an 80 °C blast drying oven. Before the test, the electrode material was immersed in 6 M KOH for 12 h so that the electrolyte ions could better diffuse into the electrode material.

In the three-electrode system, Pt and Hg/HgO electrodes were used as the counter and reference electrodes, respectively. CV and GCD tests were performed on the electrode sheet under a potential window of −1 to 0 V. The EIS measurements were conducted at an amplitude of 10 mV and a frequency of 10^{-2}–10^5 Hz. Its cycle stability (CT3002A) was tested in a LANDdt V7 test system.

The specific capacitance (C) of a single electrode was calculated by the following equation (eq 1):

$$C = \frac{I\Delta t}{m\Delta V} \tag{1}$$

where m (g) denotes the mass of the active material in the electrode, I (A) is the discharging current, and ΔV (V) represents the potential change within the discharge time Δt (s).

The Coulombic efficiency (η) was calculated by using eq 2:

$$\eta = \frac{t_d}{t_c} \tag{2}$$

where t_d (s) and t_c (s) denote the discharge and charge times, respectively.

According to the Cottrell equation, in the linear scanning process with a constant scanning rate, the electrode current is controlled by the following relationship (eqs 3 and 4):

$$i = av^b \tag{3}$$

$$\log(i) = \log(a) + b\log(v) \tag{4}$$

where i (v) denotes the current at a given action potential, v (mV s^{-1}) is the scanning rate, and a and b are constants.

In the two-electrode system, a 6 M KOH solution was used as an electrolyte, and two electrode sheets with the same mass were used as positive and negative electrodes to form a coin-shaped symmetrical device. The electrochemical tests were carried out on the electrochemical workstation and the LANDdt V7 test system. The specific capacitance of a single electrode was calculated from the GCD values according to the following equation (eq 5):

https://doi.org/10.1021/acsomega.3c02610
ACS Omega 2023, 8, 34471–34480

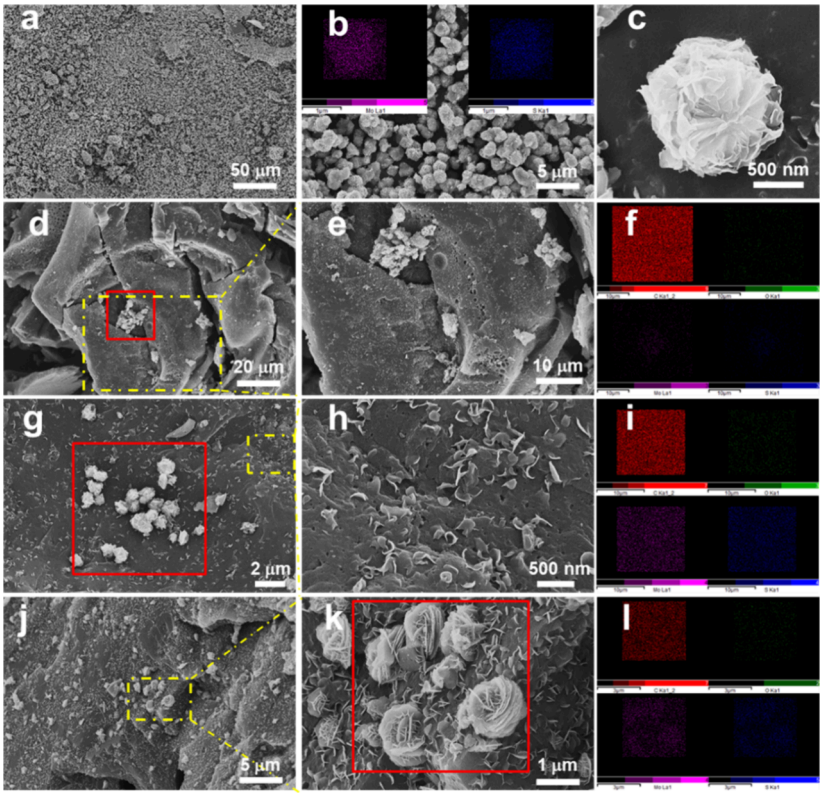

Figure 1. SEM and elemental surface distribution maps of the samples: (a–c) MoS_2, (d–f) MoS_2@PC-0.2, (g–i) MoS_2@PC-0.3, and (j–l) MoS_2@PC-0.4.

$$C = \frac{2I\Delta t}{m\Delta V} \tag{5}$$

where I (A) denotes the discharging current, m (g) is the average mass of the active material in the two electrodes, and ΔV (V) represents the potential change within the discharge time Δt (s).

The energy density (E) and power density (P) were defined using eqs 6 and 7:

$$E_t = \frac{C_t \Delta V^2}{2 \times 3.6} \tag{6}$$

$$P_t = \frac{3600 E_t}{\Delta t} \tag{7}$$

where P_t (W kg^{-1}) denotes the specific power density, E_t (W h kg^{-1}) is the specific energy density, C_t (F g^{-1}) stands for the specific capacitance, and ΔV (V) represents the potential change within the discharge time Δt (s).

3. RESULTS AND DISCUSSION

3.1. Material Characterization. Figure 1 shows the SEM and elemental plane distributions of MoS_2 and MoS_2@PC-*M*. Figure 1a shows that the prepared MoS_2 is a flower-shaped sphere with a diameter of about 2 μm assembled from MoS_2 nanosheets. The hollow structure between these nanosheets plays a great role in increasing the specific surface area of MoS_2. In addition, flower clusters of MoS_2 can be observed on all MoS_2@PC surfaces, indicating that MoS_2@PC has been successfully synthesized in the experiment (Figure 1d–l). Except for a few flower-like MoS_2 on the MoS_2@PC-0.2 surface, no other morphologies of MoS_2 were observed. However, with the increase in MoS_2 content, lamellar MoS_2 semi-embedded on the PC substrate appears on the sample surface (Figure 1g,h), which may affect the pore structure of MoS_2@PC, resulting in the reduction of the electrical double-layer capacitance provided by PC. As shown in Figure 1j,k, the lamellar MoS_2 has a very high distribution density, which may cause the storage and transportation of electrolyte ions on MoS_2@PC-0.4 to be blocked, thus affecting the electrochemical performance. The elemental plane distribution diagram shows that with the increase in MoS_2 load (Figure 1f,i,l), the distribution of the Mo element is denser. It is noteworthy that all of the elements of MoS_2@PC-0.3 are evenly distributed without obvious accumulation, which ensures the rapid transmission of electrolyte ions.

Figure 2 shows the TEM, HRTEM, lattice, and SAED images of MoS_2@PC-0.3. As shown in Figure 2a, spherical MoS_2 is formed by winding irregular sheet MoS_2, and the pores between sheets provide an additional specific surface area for the storage and transportation of electrolyte ions. Figure 2b shows that MoS_2 has clear and neat lattice stripes, indicating that the synthesized MoS_2 has high crystallinity. In addition, Figure 2c shows that the characteristic spacing of the sample lattice plane is 0.647 nm, which can be attributed to the (002) crystal plane in the 2H-MoS_2 phase (Figure 2d), which is consistent with the following XRD results.[25]

Figure 3 shows the N_2 adsorption and desorption and pore size distribution curve of MoS_2@PC-*M*. MoS_2@PC-*M* displays a type I/IV isotherm, indicating that it has a large number of micropores and a small amount of mesopores (Figure 3a). The pore size distribution in Figure 3b also further shows that the pore size of MoS_2@PC-*M* is mostly concentrated below 2 nm. The specific surface area of MoS_2@PC-0.3 calculated by DFT

https://doi.org/10.1021/acsomega.3c02610
ACS Omega 2023, 8, 34471−34480

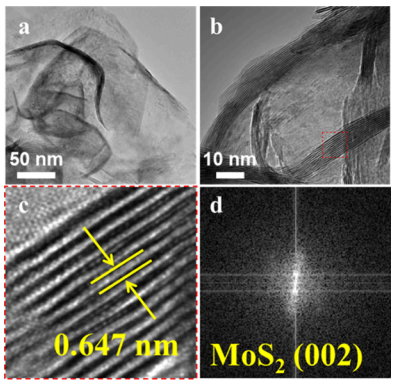

Figure 2. (a) TEM image of MoS_2@PC-0.3, (b) HRTEM image of MoS_2@PC-0.3, and (c, d) lattice and SAED pattern of MoS_2@PC-0.3.

is 3053 m^2 g^{-1}, which shows that the specific surface area of MoS_2@PC-0.3 can be improved compared with that of PC (Table 1 and Table S1). The specific surface area of MoS_2@PC-0.4 is 2258 m^2 g^{-1}, which is lower than that of PC. This indicates that when excessive MoS_2 is loaded on the surface of PC, it can cover the pore structure of part of PC, resulting in the reduction of its specific surface area. This will affect the storage and transport channels of the electrolyte ions.

Figure 4a shows the XRD spectrum of MoS_2@PC-*M*. MoS_2@PC-*M* has the (002) and (100) diffraction peaks attributed to graphite at 23 and 43°[26] and shows high intensity diffraction peaks at low angles, indicating that it has rich micropores. The diffraction peaks of the sample at 14.3 and 33.4° correspond to the (002) and (100) crystal planes of MoS_2,[27] which are consistent with the TEM analysis results. In addition, the diffraction peak intensity of XRD is proportional to the loading amount of MoS_2, whereas the diffraction peak intensity of the low angle is just the opposite, which is caused by the loading of MoS_2 blocking part of the micropores of PC. This phenomenon supports the previous speculation about the SEM results. Figure 4b shows that all samples have D and G peaks attributed to graphite near 1350 and 1595 cm^{-1}.[28] It is worth noting that MoS_2@PC-*M* retains the original graphite structure and lattice defects of PC to a certain extent, and its I_D/I_G values are around 0.9. In addition, the diffraction peak at 860 cm^{-1} can be attributed to the C−C stretching and C−C−H bending of amorphous carbon,[29] indicating that MoS_2@PC-*M* is composed of a large amount of disordered amorphous carbon.[30] The diffraction peaks of MoS_2@PC-*M* at 375 and 402 cm^{-1} correspond to the typical E^1_{2g} and A_{1g} vibration modes of the 2H-MoS_2 phase.[31]

Table 1. Textural Parameters of the Samples

sample	SSA_{BET} (m^2 g^{-1})	SSA_{mic} (m^2 g^{-1})	PV (m^3 g^{-1}) total	PV micro	D_{ap} (nm)
MoS_2@PC-0.2	2664	2527	1.31	1.14	1.97
MoS_2@PC-0.3	3053	2898	1.48	1.29	1.93
MoS_2@PC-0.4	2258	2164	1.08	0.98	1.92

Table 2 shows the elemental content of the sample obtained by XPS analysis. As can be seen, the contents of Mo and S also increase significantly with the increase in loading. Figure 5 a shows that the samples have Mo 4p, S 2p, C 1s, Mo 3d, Mo 3p, Mo 3s, and O 1s peaks with different strengths. The Mo and S peaks increase significantly with the increase in MoS_2 loading, which are consistent with the results in Table 2. Figure 5b displays the C 1s peak of MoS_2@PC-M, which can be decomposed into four peaks corresponding to different carbon bonds, namely, 284.4 eV >C−C<, 285.7 eV >C−S<, 286.6 eV >C−O−, and 289.1 eV >C═O. It can be seen that different MoS_2 loads have little effect on the carbon bond. Figure 5c shows the Mo 3d peak of MoS_2@PC-*M*. The two peaks at 229.1 and 232.2 eV in the figure correspond to the $3d_{5/2}$ and $3d_{3/2}$ peaks of the Mo−S bond of 2H phase MoS_2, respectively.[32] Because this result is consistent with the Raman result, it can be determined that MoS_2 in MoS_2@PC-*M* exists in the 2H phase. In addition, the peak strength of Mo^{6+} at 235.7 eV is weak, indicating that Mo in the composite mainly exists in the form of MoS_2, and the weak peak at 226.1 eV is caused by the S 2s peak.[33] During the process of discharging and charging, Mo^{6+} ions in MoS_2@PC-*M* can improve the oxidation and reduction between Mo and Mo^{4+}, thus improving the reversible capacity in the electrochemical cycle process.[34] Figure 5d shows the XPS spectra of S $2p_{3/2}$ and S $2p_{1/2}$ of MoS_2@PC-*M*, which are 162.0 and 163.2 eV, respectively. Caused by the Mo−S bond in MoS_2,[35] they correspond to 2H phase molybdenum disulfide and the results in Figure 5c as well.

3.2. Electrochemical Characterization. *3.2.1. Three-Electrode System.* As shown in Figure 6a, there is no obvious redox peak in the CV curve of MoS_2@PC-*M*, but a small envelope peak in the voltage range of −0.8 to −0.4 V, which is caused by the redox reaction of oxygen-containing functional

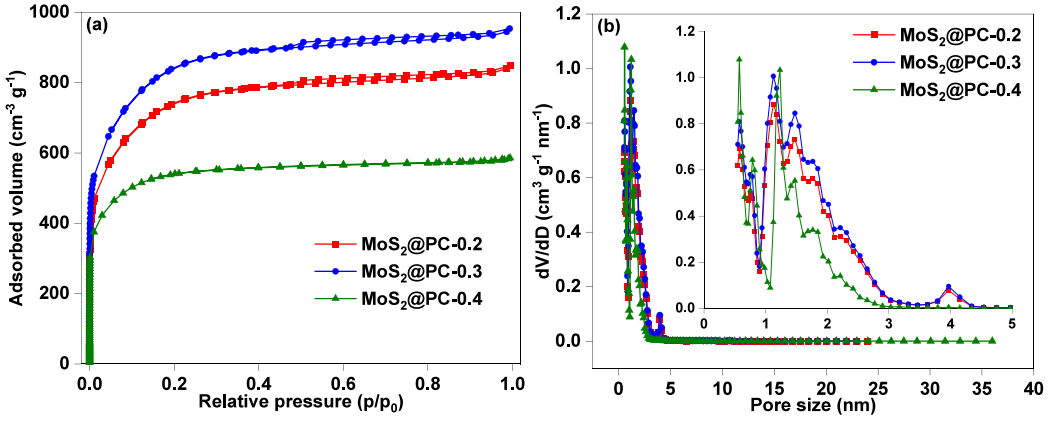

Figure 3. (a) N_2 adsorption−desorption isotherms and (b) pore size distribution curves of the samples.

https://doi.org/10.1021/acsomega.3c02610
ACS Omega 2023, 8, 34471−34480

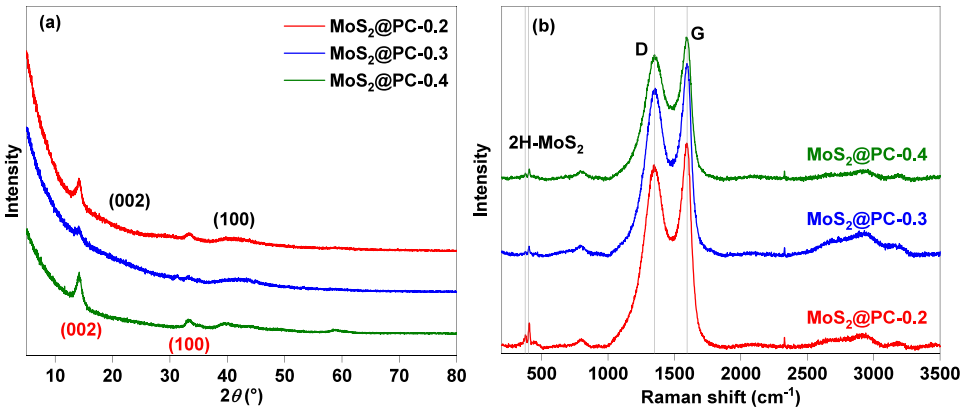

Figure 4. (a) XRD patterns of MoS_2@PC-M and (b) Raman pattern of MoS_2@PC-M.

Table 2. Elemental Content of MoS_2@PC-*M* Obtained by XPS analysis

	XPS (%)			
sample	C	Mo	O	S
MoS_2@PC-0.2	90.58	0.63	7.13	1.67
MoS_2@PC-0.3	84.87	2.59	7.77	4.76
MoS_2@PC-0.4	75.15	4.92	8.47	8.45

groups and a small amount of Mo^{6+} in the sample. The area enclosed by the CV curve can quantify the specific capacitance of the sample. It can be seen that the specific capacitance of MoS_2@PC-0.2 and MoS_2@PC-0.3 is significantly improved compared with that of PC. This is because there is less MoS_2 loaded on the surface of MoS_2@PC-0.2. On the basis of not affecting the pore structure of PC, it contributes a certain amount of pore structure and Mo^{6+}, which can cause a redox reaction, resulting in its specific capacitance being improved compared with PC. Further increasing the load of MoS_2 will not affect the original pore structure of PC, and its own pore can also provide more storage and transport space for electrolyte ions. In addition, a proper amount of oxygen-containing functional groups and the pseudocapacitance provided by Mo^{6+} make its specific capacitance significantly improved. When the PC surface is loaded with excessive MoS_2,

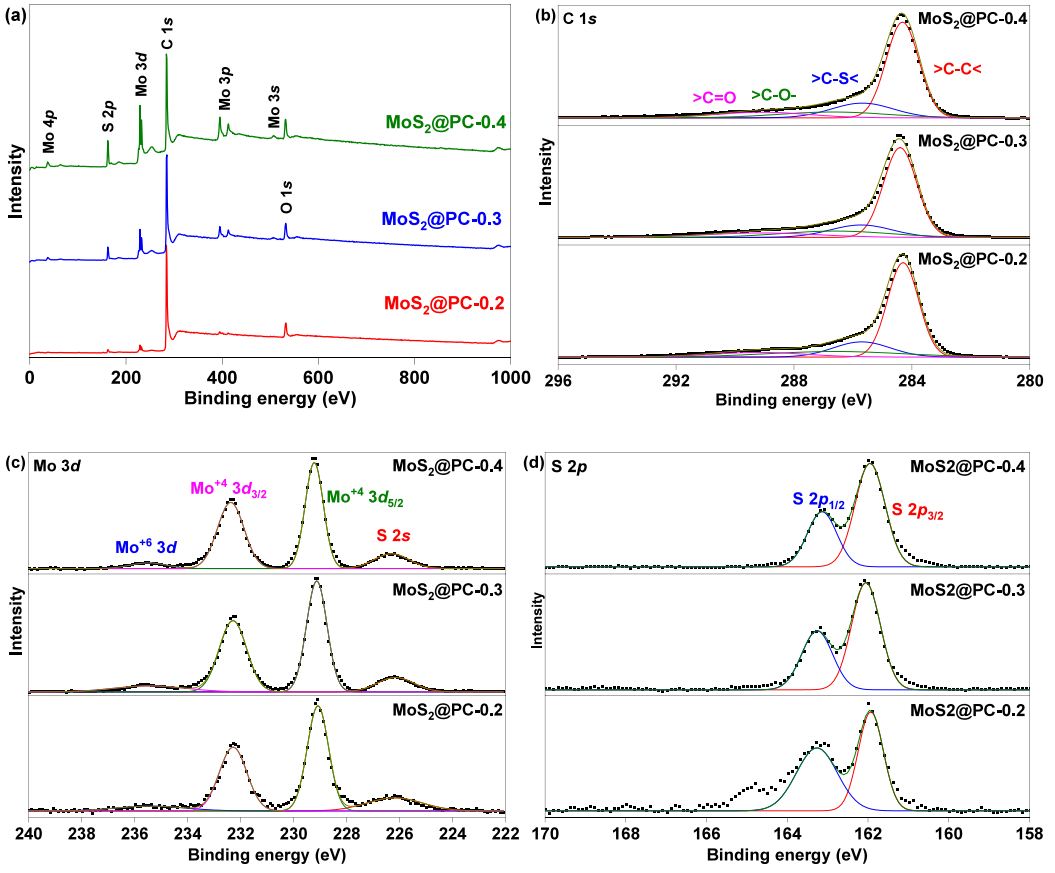

Figure 5. (a) XPS spectrum of MoS_2@PC-*M*, (b) XPS spectrum of C 1s of MoS_2@PC-*M*, (c) XPS spectrum of Mo 3d of MoS_2@PC-*M*, and (d) XPS spectrum of S 2p of MoS_2@PC-*M*.

https://doi.org/10.1021/acsomega.3c02610
ACS Omega 2023, 8, 34471−34480

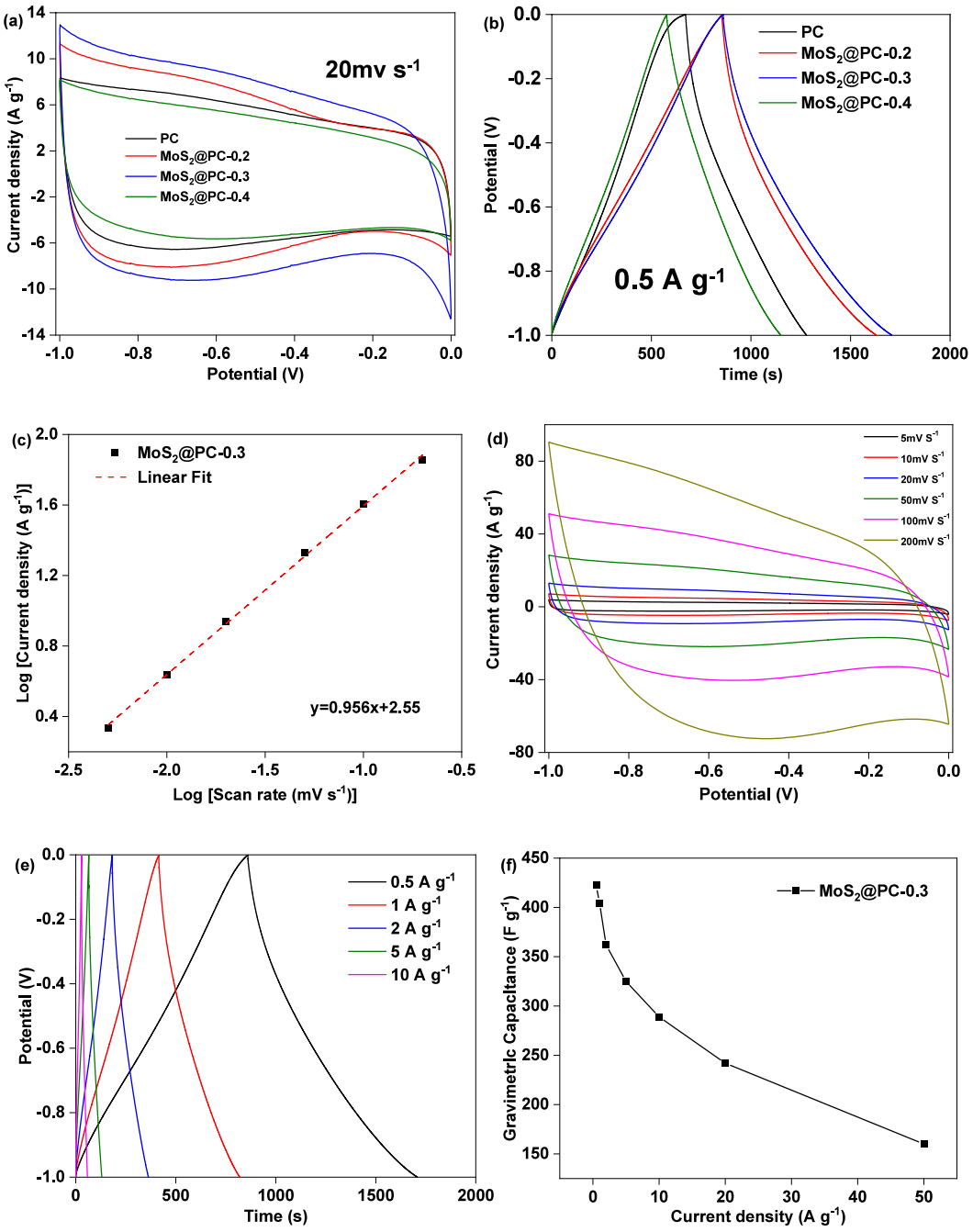

Figure 6. (a, b) CV and GCD curves of PC and MoS_2@PC-*M*, (c) slope values of the plot of current density versus scan rate obtained by linear fitting, (d) CV curves of MoS_2@PC-0.3 at different scan rates, (e) GCD curves of MoS_2@PC-0.3 at different current densities, and (f) rate performance curves of MoS_2@PC-0.3

its own pore structure will be blocked, resulting in obstruction of electrolyte ion transport, thus reducing the specific capacitance. According to Figure 6b, the specific capacitances of MoS_2@PC-0.2, MoS_2@PC-0.3, and MoS_2@PC-0.4 at 0.5 A g^{-1} current density are 387, 422.5, and 280 F g^{-1}, respectively, and the specific capacitance of MoS_2@PC-0.3 is increased by 36.4% compared with that of PC. Figure 6c shows the change relationship between the scanning rate and the logarithm of current density fitted according to eq 4. The slope of the fitting curve is close to 1, indicating that the MoS_2 PC-0.3 electrode is mainly based on the double-layer energy storage mechanism.[36]

As can be seen from Figure 6d, the CV curve of the MoS_2@PC-0.3 electrode material presents a rectangular shape at a low scanning speed. With the increase in scanning speed, the CV curve gradually presents a shuttle shape, which is due to the existence of a large number of micropores in MoS_2@PC-0.3. When the scanning speed increases, the electrolyte solution can not get in and out of the electrode material surface quickly due to the small pore size, which leads to a certain delay in the ion diffusion and leads to poor conductivity. Figure 6e,f shows the GCD curves and magnification performance diagrams of MoS_2@PC-0.3 under different current densities. Due to the increase in transmission resistance, the specific capacitance of MoS_2@PC-0.3 decreases with the increase in current density. At a current density of 20 A g^{-1}, the capacitance retention rate of MoS_2@PC-0.3 is only 57.3%. This may be due to the

https://doi.org/10.1021/acsomega.3c02610
ACS Omega 2023, 8, 34471−34480

volume change of MoS_2 during the charging and discharging process, resulting in its poor magnification performance. Table 3 describes the comparison of the specific capacitance of the

Table 3. Electrochemical Performance of the Samples

material	electrolyte	capacitance ($F\ g^{-1}$)	current density ($A\ g^{-1}$)	reference
MoS_2/C(corncobs)	1 M Na_2SO_4	333.5	1	21
flower-like MoS_2/C	1 M Na_2SO_4	201.4	0.2	37
MoS_2/activated carbon	0.5 M H_2SO_4	261	2 mV s^{-1}	22
MoS_2-graphene	1 M Na_2SO_4	243	1	38
MoS_2@C nanofiber	6 M KOH	355.6	5 mV s^{-1}	37
MoS_2/RCF electrode	3 M KOH	225	0.5	39
ACFTs/MoS_2	1 M Na_2SO_4	308.5	5 mV s^{-1}	40
C/MoS_2 composites	3 M KOH	210	1	41
MoS_2/C(cornstalks)	1 M Na_2SO_4	338.3	1	42
MoS_2@PC-0.3	6 M KOH	422.5	0.5	this work

MoS_2-based and biomass-derived porous carbon electrodes in different electrolytes. It can be found that the MoS_2@PC-0.3 composite had a higher specific capacity.

To study the impedance of the composite materials, EIS tests were carried out on PC and MoS_2@PC-*M*. Figure 7 shows the AC impedance spectrum of PC and MoS_2@PC-M with a voltage of 10 mV in the frequency range 10^{-2}−10^5 Hz. As can be seen, the R_c value of MoS_2@PC-0.3 is about 0.3, while the R_c value of PC is 0.63, twice that of MoS_2@PC-0.3. The semicircle diameter of MoS_2@PC-M in the high-frequency region is also much smaller than that of PC, which indicates that the R_{ct} value of MoS_2@PC-0.3 is low. It indicates that MoS_2@PC-*M* has a low charge transfer resistance, which allows electrolyte ions to be stored and released to the electrode surface quickly.[43] In addition, Figure 7b shows that MoS_2@PC-0.3 has a low relaxation time constant, which ensures that electrolyte ions can quickly penetrate into electrode materials, making it have good capacitance and fast charging capacity.[44] The phase angle of MoS_2@PC-0.3 at the minimum frequency is about −63°, indicating that the electrode material of MoS_2@PC-0.3 is mainly dual-capacitor energy storage, supplemented by the pseudocapacitor energy storage mechanism.[36] Figure 7c shows that the capacitance retention rate of MoS_2@PC-0.3 is 76.73% and the Coulombic efficiency is 100% after 10,000 cycles of charging and discharging. The poor cycling stability is due to the loss of MoS_2 during charge and discharge. Based on this, we intend to solve this scientific problem by wrapping carbon materials in the following work.

3.2.2. MoS_2@PC-M Symmetric SCs. To further explore the electrochemical performance of the MoS_2@PC-*M* electrode material, two electrode materials of the same quality were used as positive and negative electrodes for the two-electrode system test. Figure 8 shows that the CV curves of MoS_2@PC-*M* display a rectangular shape, indicating that MoS_2@PC-*M* mainly stores and transports electrons through the pore structure. It is worth noting that there is a small envelope peak in the voltage range of 0.4−0.8, which is due to the existence of Mo^{6+} in MoS_2@PC-*M*. It can induce the redox reaction to form a redox peak, thus providing pseudocapacitance. With the increase in scanning rate, the CV curve of MoS_2@PC-0.3 does not change significantly, indicating that it has high reversibility, good electrochemical activity, and stable voltage window (Figure 8b). As can be seen from Figure 8c, the shape of the GCD curve of MoS_2@PC-*M* slightly deviates from the isosceles triangle. It indicates that the capacitance contribution of the sample is mainly double-layer capacitance, supplemented by pseudocapacitance, which is consistent with the CV result. The specific capacitances of MoS_2@PC-0.2, MoS_2@PC-0.3, and MoS_2@PC-0.4 at 0.5 A g^{-1} are 126.0, 321.4, and 232.3 F g^{-1}, respectively, in the two-electrode system; MoS_2@PC-0.3 is 59.7% higher than that of PC (Figure S3). Figure 8d shows the GCD curve of MoS_2@PC-0.3 under different current densities. As can be seen, when the current density increases, the GCD curve has no obvious IR value, indicating that the MoS_2@PC-0.3 electrode material has good magnification performance.[45] Figure 8e shows the relationship between the energy density of MoS_2@PC-0.3 and the power density. When the power density is 500.0 W kg^{-1}, the energy density is 44.6 W h^{-1} kg^{-1}. Even at a high power density of 9998.6 W kg^{-1}, the energy density is still 31.94 W h^{-1} kg^{-1}. The energy density of MoS_2@PC-0.3 is much higher than that of PC, which indicates that the load of MoS_2 can greatly improve the energy density of PC. Figure 8f shows that the capacitance retention rate of MoS_2@PC-0.3 after 10,000 charge−discharge cycles is up to 87.69%, and the Coulombic efficiency is 100%.

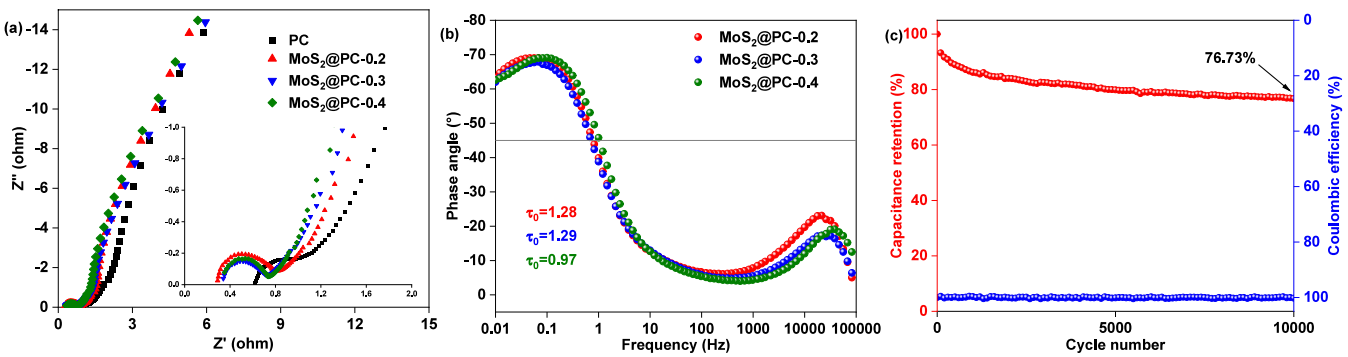

Figure 7. (a) Nyquist plot and the inset showing details in the high-frequency range of MoS_2@PC-*M* and PC, (b) relationship between phase angle and frequency of MoS_2@PC-*M*, and (c) cyclic performance and Coulombic efficiency plots of MoS_2@PC-0.3

https://doi.org/10.1021/acsomega.3c02610
ACS Omega 2023, 8, 34471−34480

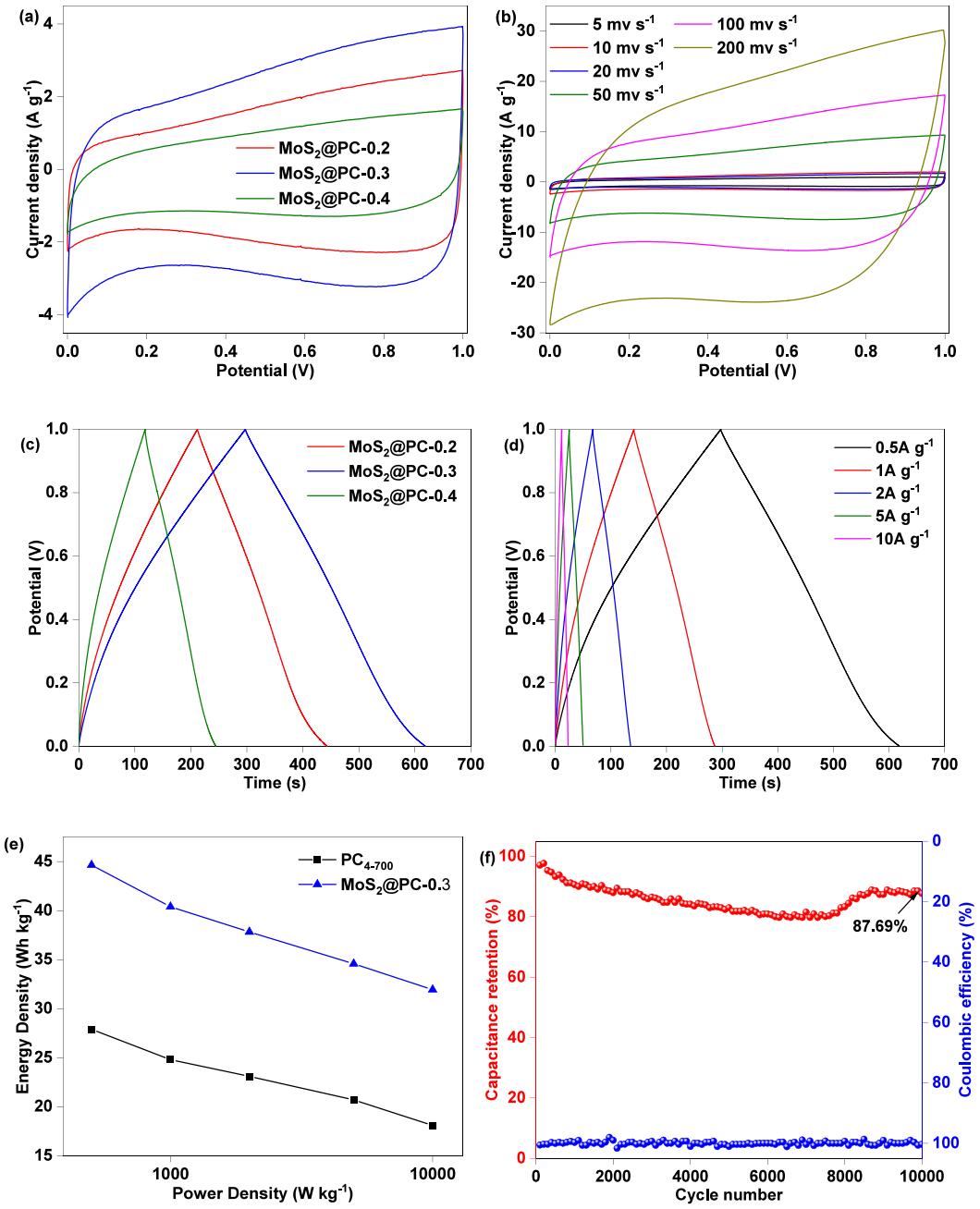

Figure 8. Electrochemical properties of samples in the two-electrode system: (a) CV curves of MoS_2@PC-*M*, (b) CV curves of MoS_2@PC-0.3 at different scan rates, (c) GCD curves of MoS_2@PC-*M*, (d) GCD curves of MoS_2@PC-0.3 at different current densities, (e) relationship between power density and energy density of MoS_2@PC-0.3, and (f) cycling performance and Coulombic efficiency of MoS_2@PC-0.3 at 20 A g^{-1}.

4. CONCLUSIONS

In this paper, MoS_2@PC was prepared by the hydrothermal method with self-made PC as the substrate, ammonium molybdate as the molybdenum source, and thiourea as the sulfur source. The effects of different MoS_2 loadings on the morphology, structure, and electrochemical properties of MoS_2@PC were studied. Among them, MoS_2@PC-0.3 displays good electrochemical performance due to the appropriate MoS_2 load. The pore structure of MoS_2@PC provides sufficient attachment sites and diffusion channels for the storage and transportation of the electrolyte ions. In addition, the loading of MoS_2 not only greatly increases the specific surface area of the material but also enhances the additional redox reaction. It provides a pseudocapacitor energy storage mechanism and improves the energy density of PC accordingly. In the three-electrode system with 6 M KOH as the electrolyte, MoS_2@PC-0.3 shows the highest specific capacitance (422.5 F g^{-1} at 0.5 A g^{-1}), which is 36.4% higher than that of PC. In the double-electrode system, the specific capacitance of MoS_2@PC-0.3 at a current density of 0.5 A g^{-1} is 321.4 F g^{-1}. At a current density of 20 A g^{-1}, the capacitance retention rate is 87.69% after 10,000 cycles, and the Coulombic efficiency is 100%. In addition, the power density provided by the MoS_2@PC-0.3 electrode is 500.0 W kg^{-1}, and the energy density can reach 44.6 W h kg^{-1}. When the power density is 9998.6 W kg^{-1}, the energy density is still 31.9 W h kg^{-1}. It shows that the load of MoS_2 greatly improves the energy density of PC. Therefore, this paper provides a simple,

https://doi.org/10.1021/acsomega.3c02610
ACS Omega 2023, 8, 34471−34480

green, and economic strategy for large-scale preparation of MoS_2@PC using coal tar pitch-based PC as a precursor for SCs.

■ ASSOCIATED CONTENT

Supporting Information

The Supporting Information is available free of charge at https://pubs.acs.org/doi/10.1021/acsomega.3c02610.

Preparation of PC; nitrogen adsorption and desorption and pore size distribution diagram; textural parameters of the samples; elemental content obtained by EDS analysis; TG curve; CV and GCD curves (PDF)

■ AUTHOR INFORMATION

Corresponding Author

Cui-Ying Lu − *Shaanxi Key Laboratory of Low Metamorphic Coal Clean Utilization, School of Chemistry and Chemical Engineering, Yulin University, Yulin, Shaanxi 719000, China*; Phone: +86 0912 3891144; Email: lucuiying126@126.com; Fax: +86 0912 3891144

Authors

Rui Bai − *Shaanxi Key Laboratory of Low Metamorphic Coal Clean Utilization, School of Chemistry and Chemical Engineering, Yulin University, Yulin, Shaanxi 719000, China*; orcid.org/0000-0001-5642-1670

Yuan-Jia Cao − *Yulin Zhongke Innovation Institute For Clean Energy, Yulin, Shaanxi 719000, China*

Guang-Hui Liu − *Shaanxi Key Laboratory of Low Metamorphic Coal Clean Utilization, School of Chemistry and Chemical Engineering, Yulin University, Yulin, Shaanxi 719000, China*; orcid.org/0000-0003-0650-3875

Complete contact information is available at: https://pubs.acs.org/10.1021/acsomega.3c02610

Notes

The authors declare no competing financial interest.

■ ACKNOWLEDGMENTS

The study was supported by the Joint Fund Project of Yulin University-Dalian National Laboratory for Clean Energy (Grant YLU-DNL Fund 2021009, 2021015 and 2022012), the National Natural Science Foundation of China (nos. 42362023), the Shaanxi Province Education Department Key Scientific Research Project (21JS046), and the Industry University Research Cooperation Project of Yulin (CXY202110301).

■ REFERENCES

(1) Simon, P.; Gogotsi, Y. Materials for electrochemical capacitors. *Nat. Mater.* **2008**, *7*, 845−854.

(2) Zhang, Q.; Liu, Z.; Zhao, B.; Cheng, Y.; Zhang, L.; Wu, H. H.; Wang, M. S.; Dai, S.; Zhang, K.; Ding, D.; Wu, Y.; Liu, M. Design and understanding of dendritic mixed-metal hydroxide emailprotected carbon nanotube array electrode for high-performance asymmetric supercapacitors. *Energy Storage Mater.* **2019**, *16*, 632−645.

(3) Dai, S.; Zhao, B.; Qu, C.; Chen, D.; Dang, D.; Song, B.; deGlee, B. M.; Fu, J.; Hu, C.; Wong, C. P.; Liu, M. Controlled synthesis of three-phase NixSy/rGO nanoflake electrodes for hybrid supercapacitors with high energy and power density. *Nano Energy* **2017**, *33*, 522−531.

(4) Kyriakopoulos, G. L.; Arabatzis, G. Electrical energy storage systems in electricity generation: Energy policies, innovative technologies, and regulatory regimes. *Renewable Sustainable Energy Rev.* **2016**, *56*, 1044−1067.

(5) Yu, P.; Liang, Y.; Dong, H.; Hu, H.; Liu, S.; Peng, L.; Zheng, M.; Xiao, Y.; Liu, Y. Rational Synthesis of Highly Porous Carbon from Waste Bagasse for Advanced Supercapacitor Application. *ACS Sustainable Chem. Eng.* **2018**, *6*, 15325−15332.

(6) Wei, J. S.; Wan, S.; Zhang, P.; Ding, H.; Chen, X. B.; Xiong, H. M.; Gao, S.; Wei, X. Preparation of porous carbon electrodes from semen cassiae for high-performance electric double-layer capacitors. *New. J. Chem.* **2018**, *42*, 6763−6769.

(7) Yu, F.; Huang, T.; Zhang, P.; Tao, Y.; Cui, F. Z.; Xie, Q.; Yao, S.; Wang, F. Design and synthesis of electrode materials with both battery-type and capacitive charge storage. *Energy Storage Mater.* **2019**, *22*, 235−255.

(8) Muzaffar, A.; Ahamed, M. B.; Deshmukh, K.; Thirumalai, J. A review on recent advances in hybrid supercapacitors: Design, fabrication and applications. *Renewable Sustainable Energy Rev.* **2019**, *101*, 123−145.

(9) Fic, K.; Platek, A.; Piwek, J.; Frackowiak, E. Sustainable materials for electrochemical capacitors. *Mater. Today* **2018**, *21*, 437−454.

(10) Tang, C.; Zhong, L.; Zhang, B.; Wang, H. F.; Zhang, Q. 3D Mesoporous van der Waals Heterostructures for Trifunctional Energy Electrocatalysis. *Adv. Mater.* **2018**, *30*, No. 1705110.

(11) Zhang, R.; Dong, Y.; Al-Tahan, M. A.; Zhang, Y.; Wei, R.; Ma, Y.; Yang, C.; Zhang, J.; et al. Insights into the sandwich-like ultrathin Ni-doped MoS_2/rGO hybrid as effective sulfur hosts with excellent adsorption and electrocatalysis effects for lithium-sulfur batteries. *J. Energy Chem.* **2021**, *60*, 85−94.

(12) Wei, S.; Zhou, R.; Wang, G. Enhanced Electrochemical Performance of Self-Assembled Nanoflowers of MoS_2 Nanosheets as Supercapacitor Electrode Materials. *ACS Omega* **2019**, *4*, 15780−15788.

(13) Acerce, M.; Voiry, D.; Chhowalla, M. Metallic 1T phase MoS_2 nanosheets as supercapacitor electrode materials. *Nat. Nanotechnol.* **2015**, *10*, 313−318.

(14) Clerici, F.; Fontana, M.; Bianco, S.; Serrapede, M.; Perrucci, F.; Ferrero, S.; Tresso, E.; Lamberti, A. In situ MoS_2 Decoration of Laser-Induced Graphene as Flexible Supercapacitor Electrodes. *ACS Appl. Mater. Interfaces* **2016**, *8*, 10459.

(15) Kai, W.; Liwei, L.; Wen, X.; Shengzhe, Z.; Yong, L.; Hongwei, Z.; Zongqiang, S. Electrodeposition Synthesis of PANI/MnO_2/Graphene Composite Materials and its Electrochemical Performance. *Int. J. Electrochem. Sci.* **2017**, *12*, 8306−8314.

(16) Wang, K.; Li, L.; Zhang, T.; Liu, Z. Nitrogen-doped graphene for supercapacitor with long-term electrochemical stability. *Energy* **2014**, *70*, 612−617.

(17) Xia, G. T.; Li, C.; Wang, K.; Li, L. W. Structural Design and Electrochemical Performance of PANI/CNTs and MnO_2/CNTs Supercapacitor. *Sci. Adv. Mater.* **2019**, *11*, 1079−1086.

(18) Tiwari, P.; Jaiswal, J.; Chandra, R. Hierarchal growth of MoS_2@CNT heterostructure for all solid state symmetric supercapacitor: Insights into the surface science and storage mechanism. *Electrochim. Acta* **2019**, *324*, No. 134767.

(19) Fu, G.; Ma, L.; Gan, M.; Zhang, X.; Jin, M.; Lei, Y.; Yang, P.; Yan, M. Fabrication of 3D spongia-shaped polyaniline/MoS_2 nanospheres composite assisted by polyvinylpyrrolidone (PVP) for high-performance supercapacitors. *Synth. Met.* **2017**, *224*, 36−45.

(20) Lin, Q. J.; Wang, J. M.; Chen, J. H.; Yang, Q.; Fang, L. J.; Huang, Y. D. Collaborative improvement electrochemical properties of supercapacitor electrodes by loading MoS_2 nanosheets on biomass hierarchical porous carbon. *J. Electrochem. Soc.* **2022**, *169*, No. 020502.

(21) Wang, F.; Ma, J.; Zhou, K.; Li, X. MoS_2/corncob-derived activated carbon for supercapacitor application. *Mater. Chem. Phys.* **2020**, *244*, No. 122215.

(22) Sangeetha, D. N.; Selvakumar, M. Active-defective activated carbon/MoS_2 composites for supercapacitor and hydrogen evolution reactions. *Appl. Surf. Sci.* **2018**, *453*, 132−140.

(23) Lin, M.; Deng, M.; Zhou, C.; Shu, Y.; Yang, L.; Ouyang, L.; Gao, Q.; Zhu, M. Popcorn derived carbon enhances the cyclic stability of MoS_2 as an anode material for sodium-ion batteries. *Electrochim. Acta* **2019**, *309*, 25−33.
(24) Cao, Y. J.; Lu, C. Y.; Zhang, Z. W.; Wang, Z.; Kang, Y. H.; Yang, T. T.; Liu, G. H.; Wei, X. Y.; Bai, H. C. N/O Co-doped porous carbons derived from coal tar pitch for ultra-high specific capacitance supercapacitors. *ACS Omega* **2022**, *27*, 23342−23352.
(25) Mahajan, H.; Mohanan, K. U.; Cho, S. Facile synthesis of biocarbon-based MoS_2 composite for high-performance supercapacitor application. *Nano lett.* **2022**, *22*, 8161−8167.
(26) Cui, H.; Shi, J.; Xu, J.; Yan, N.; Liu, Y. Direct synthesis of N, S co-doped porous carbons using novel organic potassium salts as activators for efficient CO_2 adsorption. *Fuel* **2023**, *342*, No. 127824.
(27) Zhu, J.; Sun, W.; Yang, D.; Zhang, Y.; Hoon, H. H.; Zhang, H.; Yan, Q. Multifunctional architectures constructing of PANI nanoneedle arrays on MoS_2 thin nanosheets for high-energy supercapacitors. *Small* **2015**, *11*, 4123−4129.
(28) Yoshikawa, Y.; Teshima, K.; Futamura, R.; Tanaka, H.; Neimark, A. V.; Kaneko, K.; et al. Structural mechanism of reactivation with steam of pitch-based activated carbon fibers. *J. Colloid Interface Sci.* **2020**, *578*, 422−430.
(29) Movasaghi, Z.; Rehman, S.; Rehman, I. U. Raman spectroscopy of biological tissues. *Appl. Spectrosc. Rev.* **2007**, *5*, 493−541.
(30) Rahmatinejad, J.; Liu, X.; Zhang, X.; Raisi, B.; Ye, Z. Embedding amorphous MoS_x within hierarchical porous carbon by facile one-pot synthesis for superior sodium ion storage. *J. Energy Chem.* **2022**, *75*, 240.
(31) Wang, H.; Lu, Z.; Xu, S.; Kong, D.; Cha, J. J.; Zheng, G.; Hsu, P. C.; Yan, K.; Bradshaw, D.; Prinz, F. B.; Cui, Y. Electrochemical tuning of vertically aligned MoS_2 nanofilms and its application in improving hydrogen evolution reaction. *Proc. Natl. Acad. Sci. U.S.A.* **2013**, *110*, 19701−19706.
(32) Li, Y.; Liang, Y.; Robles Hernandez, F. C.; Yoo, H. D.; An, Q.; Yao, Y. Enhancing sodium-ion battery performance with interlayer-expanded MoS_2−PEO nanocomposites. *Nano Energy* **2015**, *15*, 453−461.
(33) Yang, Y.; Fei, H.; Ruan, G.; Xiang, C.; Tour, J. M.; et al. Edge-Oriented MoS_2 nanoporous films as flexible electrodes fo hydrogen evolution reactions and supercapacitor devices. *Adv. Mater.* **2014**, *26*, 8163−8168.
(34) Guo, J.; Zhu, H.; Sun, Y.; Tang, L.; Zhang, X. Boosting the lithium storage performance of MoS_2 with graphene quantum dots. *J. Mater. Chem. A* **2016**, *4*, 4783−4789.
(35) Long, H.; Harley-Trochimczyk, A.; Pham, T.; Tang, Z.; Shi, T.; Zettl, A.; Carraro, C.; Worsley, M. A.; Maboudian, R. High surface area MoS_2/graphene hybrid aerogel for ultrasensitive NO_2 detection. *Adv. Funct. Mater.* **2016**, *26*, 5158−5165.
(36) Tiwari, P.; Janas, D.; Chandra, R. Self-standing MoS_2/CNT and MnO_2/CNT one dimensional core shell heterostructures for asymmetric supercapacitor application. *Carbon* **2021**, *177*, 291−303.
(37) Fan, L. Q.; Liu, G. J.; Zhang, C. Y.; Wu, J. H.; Wei, Y. L. Facile one-step hydrothermal preparation of molybdenum disulfide/carbon composite for use in supercapacitor. *Int. J. Hydrogen Energy* **2015**, *40*, 10150−10157.
(38) Huang, K. J.; Wang, L.; Liu, Y. J.; Liu, Y. M.; Wang, H. B.; Gan, T.; Wang, L. L. Layered MoS_2−graphene composites for supercapacitor applications with enhanced capacitive performance. *Int. J. Hydrogen Energy* **2013**, *38*, 14027−14034.
(39) Kumuthini, R.; Ramachandran, R.; Therese, H. A.; Wang, F. Electrochemical properties of electrospun MoS_2@C nanofiber as electrode material for high-performance supercapacitor application. *J. Alloys Compd.* **2017**, *705*, 624−630.
(40) Gao, L.; Li, X.; Li, X.; Cheng, J.; Wang, B.; Wang, Z.; Li, C.; et al. A coaxial yarn electrode based on hierarchical MoS_2 nanosheets/carbon fiber tows for flexible solid-state supercapacitors. *RSC Adv.* **2016**, *6*, 57190−57198.
(41) Hu, B.; Qin, X.; Asiri, A. M.; Alamry, K. A.; Al-Youbi, A. O.; Sun, X. Synthesis of porous tubular C/MoS_2 nanocomposites and their application as a novel electrode material for supercapacitors with excellent cycling stability. *Electrochim. Acta* **2013**, *100*, 24−28.
(42) Zhao, G.; Cheng, Y.; Sun, P.; Ma, W.; Hao, S.; Wang, X.; Xu, X.; Xu, Q.; Liu, M.; et al. Biocarbon based template synthesis of uniform lamellar MoS_2 nanoflowers with excellent energy storage performance in lithium-ion battery and supercapacitors. *Electrochim. Acta* **2020**, *331*, No. 135262.
(43) Zhao, H.; Xing, B.; Zhang, C.; Huang, G.; Liu, Q.; Yi, G.; Jia, J.; Ma, M.; Chen, Z.; Zhang, C. Efficient synthesis of nitrogen and oxygen co-doped hierarchical porous carbons derived from soybean meal for high-performance supercapacitors. *J. Alloys Compd.* **2018**, *766*, 705−715.
(44) He, X.; Geng, Y.; Qiu, J.; Zheng, M.; Zhang, X.; Shui, H. Influence of KOH/Coke Mass Ratio on Properties of Activated Carbons Made by Microwave-Assisted Activation for Electric Double-Layer Capacitors. *Energy Fuels* **2010**, *24*, 3603−3609.
(45) Ma, H.; Chen, H.; Wu, M.; Chi, F.; Liu, F.; Bai, J.; Cheng, H.; Li, C.; Qu, L. Maximization of spatial charge density: An approach to ultrahigh energy density of capacitive charge storage. *Angew. Chem. Int. Ed.* **2020**, *132*, 14649−14657.

https://doi.org/10.1021/acsomega.3c02610
ACS Omega 2023, 8, 34471−34480